Dicle University
Journal of Engineering
https://dergipark.org.tr/tr/pub/dumf
duje.dicle.edu.tr

Research Article

AI-Driven 2D Electric Field Distribution Estimation in a Human Breast Model Formed by a Line Source

Toygar TANYEL[1], Cemanur AYDINALP[2], Gulsah YILDIZ[3]

[1] Istanbul Technical University, Electronics and Communication Engineering Department, tanyel23@itu.edu.tr, Orcid No: 0000-0002-2421-6880
[2] Istanbul Technical University, Electronics and Communication Engineering Department, aydinalp16@itu.edu.tr, Orcid No: 0000-0002-3070-6202
[3] Istanbul Technical University, Electronics and Communication Engineering Department, gulsahyildiz@itu.edu.tr, Orcid No: 0000-0002-2082-0458

ARTICLE INFO

Article history:

Received 16 August 2025
Received in revised form 13 February 2026
Accepted 23 June 2026
Available online 10 July 2026

Keywords:

Deep learning, electric field distribution estimation, dielectric properties, microwave hyperthermia, microwave imaging

Doi: 10.24012/dumf.1766927

* Corresponding author

ABSTRACT

This study addresses the computational challenges of estimating two-dimensional electric field (EF) distributions within heterogeneous breast tissue models, a critical task in medical applications such as microwave imaging and hyperthermia. Traditional numerical simulation methods are accurate but computationally expensive, often requiring hours of processing time. To overcome this limitation, we propose a deep learning approach that predicts EF distributions directly from dielectric property maps, specifically electrical conductivity and permittivity, significantly reducing inference time to a matter of seconds. Two convolutional neural network architectures are evaluated: a U-Net model with a ResNeXt50 encoder (R50-UNet) and a standard ResNeXt50 model (R50). Additionally, we introduce a masking-based loss function that emphasizes learning in regions of highest relevance within the domain. Quantitative evaluation demonstrates that the R50-UNet model outperforms the standard R50 model, achieving up to a 14.66 dB improvement in signal-to-noise ratio (SNR). The application of the masking method further enhances performance, with an additional gain of up to 3.24 dB in SNR. Data efficiency analysis reveals that while the R50 model reaches performance saturation with only 25% of the available training data, the R50-UNet architecture combined with masked loss continues to improve as more data are utilized. These findings support the feasibility of using deep learning for fast and accurate EF prediction in biomedical scenarios where computation time and spatial precision are critical.

Introduction

Electromagnetic waves are fundamental to many scientific and technological applications, as they enable the transmission of energy and information through both space and various materials. In the medical domain, these applications are particularly significant due to the non-invasive nature of diagnostic techniques such as magnetic resonance imaging (MRI), microwave imaging, and computed tomography (CT), as well as therapeutic procedures including radiofrequency ablation, microwave hyperthermia, and transcranial magnetic stimulation [1–5].

A fundamental aspect of employing electromagnetic methods in medical applications is understanding the electric field (EF) distribution within biological tissues. Therefore, it is possible to achieve accurate imaging, deliver effective treatment, and ensure safety through assessments such as the specific absorption rate (SAR) [6–8]. Although analytical models for EF computation exist, they are generally inadequate for representing the complex and heterogeneous structures found in real-world biomedical applications. Consequently, numerical methods have become indispensable tools, as they enable the simulation of complex geometries and spatially varying material properties. However, these advantages come with the drawback of high computational cost and extended simulation times, especially when high accuracy is required [9]. In clinical applications, where hardware setups are generally constant and variations stem from patient anatomy, there is an increasing need for efficient modeling approaches that can adapt to changing tissue properties. Meeting this need is challenging due to the complex electromagnetic behavior of biological tissues and the inevitable information loss introduced by the simplifications required for analytically solving Maxwell's equations.

In this study, we propose a deep learning-based framework for the rapid and accurate prediction of two-dimensional EF distributions in biological tissue. The model takes spatial dielectric properties—electrical conductivity (σ) and permittivity (ϵ) —as input, aiming to provide anatomically-informed EF predictions that enhance the efficiency and clinical usability of electromagnetic simulations. The contributions of this work can be listed as follows:

- A novel deep learning-based approach is proposed for predicting two-dimensional EF distributions directly from dielectric property maps. This method eliminates the need for iterative electromagnetic solvers and significantly reduces

computation time, making it highly efficient. The study evaluated the predicted real-valued x-component of the EF.

- To evaluate the proposed approach without depending on advanced architectural tuning, two representative deep learning models are compared: a U-Net with a ResNeXt-50 encoder and a stand-alone ResNeXt-50 network. This comparison underscores the differences between encoder–decoder and purely sequential designs, with performance assessed using root mean square error (RMSE), mean absolute error (MAE), and Signal-to-Noise Ratio (SNR) metrics.
- In order to align the learning process with the anatomical data, a masking-based loss function is employed. This approach increases learning efficiency by limiting training to only the tissue regions and prevents the model from being affected by irrelevant background areas.
- Finally, the proposed method demonstrates strong clinical relevance by offering a practical solution for real-time EF estimation. The results are valuable in personalized therapeutic applications such as microwave hyperthermia and ablation, where both computational speed and predictive accuracy are critical.

Related Works

Traditional numerical methods, such as the Finite Difference Method (FDM), Finite Element Method (FEM), and Method of Moments (MoM), are extensively used to compute EF distributions [10-12]. Although these methods provide high accuracy, their computational complexity often restricts their use in real-time clinical applications and in cases requiring detailed anatomical information.

To address the limitations of traditional applications, deep learning approaches have emerged as promising alternatives. Unlike conventional inverse problem-solving techniques in microwave dielectric characterization, which rely on iterative or heuristic optimization and often suffer from convergence issues caused by local minima, deep learning methods enable fast, non-iterative prediction of electromagnetic properties. Moreover, they eliminate the need for repeated advanced problem evaluations, by reducing computational demands. Recent studies have demonstrated their feasibility and effectiveness in this context [13–14]. For instance, a deep learning model capable of accurately predicting the near-field and far-field responses of plasmonic and dielectric nanostructures has been introduced, offering substantial speed improvements over traditional finite-difference time-domain (FDTD) simulations [15]. Similarly, in [16], various deep learning architectures (Tailored Convolutional Neural Networks (TCNN), Fully Connected Neural Networks (FCNN), and Denoising Convolutional Neural Networks (DnCNN)) are utilized to demonstrate high predictive accuracy for EF distributions in nanoparticles and array structures.

Additional studies by Yao et. al employed deep convolutional neural networks (DConvNets and DRCNNs) to predict EF distributions using MNIST datasets [17, 18]. These works modeled Green's functions for cylindrical geometries under both single- and multi-frequency conditions. Although these approaches have shown effectiveness of the model, their reliance on indirect representations of dielectric properties restricts their applicability to anatomically complex tissues.

In the field of medical imaging, deep residual networks—particularly ResNet and U-Net variants—have shown strong performance [19-22]. For instance, ResNet-18 demonstrated robust generalization across diverse modalities including MRI, CT, PET, and mammography [19], while deeper architectures such as ResNet-50 offered improved resilience in complex classification tasks [20]. ResNeXt, an extension of this family, further enhances representational power through aggregated residual transformations and increased cardinality [21]. U-Net, a widely adopted architecture for biomedical image segmentation, is particularly effective due to its symmetric encoder-decoder design, which captures both contextual and spatial features—even when trained on relatively small datasets [22].

In this work, as well as utilizing the ResNeXt50 architecture itself, we integrated a hybrid U-Net model with a ResNeXt50 encoder, combining the contextual precision of U-Net with the enhanced feature extraction capabilities of ResNeXt to achieve accurate and robust EF predictions. For simplicity, these architectures will be referred as R50 and R50-UNet. To evaluate this approach, anatomically realistic MRI-derived datasets of the human breast, developed at the University of Wisconsin–Madison, were employed [23]. These phantoms incorporate heterogeneous anatomical structures and frequency-dependent dielectric properties that closely mimic in vivo conditions, thereby providing a reliable testbed for clinical relevance. Consequently, the proposed method supports the development of clinically meaningful electromagnetic models. By uniting advanced neural network architectures with biologically informed loss functions, the framework improves predictive accuracy while maintaining computational efficiency, strengthening its potential for translation into clinical applications.

Material and Methods

This study utilizes R50-UNet and R50 architectures to predict EF distributions. First section details the data generation process and later section describes the deep learning model architectures, masking strategies, and evaluation metrics. The experiments were conducted on a system equipped with a 14th-generation Intel Core i9-14900KF processor (3.20 GHz), an NVIDIA GeForce RTX 4090 GPU, and running Windows 11. Model implementation and training were performed using Python 3.9.21 and PyTorch 2.5.1.

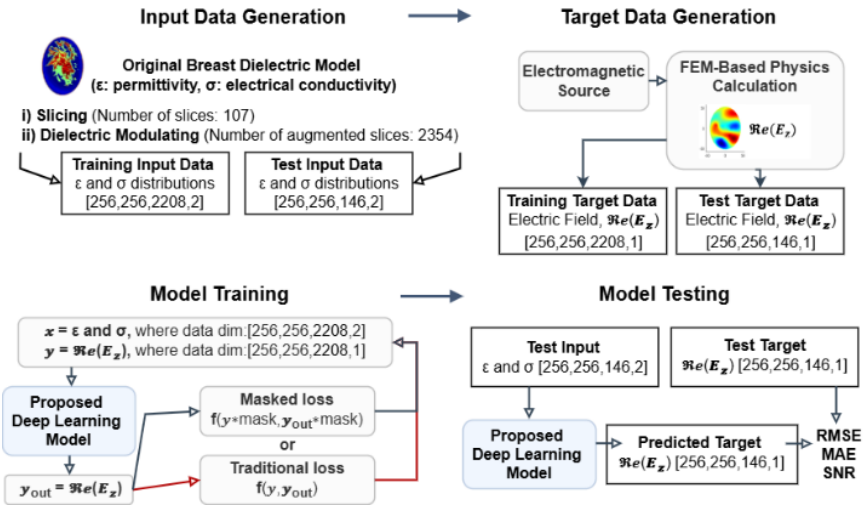

Figure 1. Methodological pipeline for deep learning-based estimation of electric field (EF) distributions in breast tissue using dielectric property maps. The workflow comprises four major components: Input Data Generation, Target Data Generation, Model Training, and Model Testing.

Dataset

Breast density is generally categorized into four classes based on the proportion of fibroglandular tissue: mostly fatty, scattered fibroglandular, heterogeneously dense, and very dense. For microwave hyperthermia applications, breast tissue composition is critical since adipose and fibroglandular tissues has different dielectric properties ($\varepsilon_r \approx 4$ for adipose tissue and $\varepsilon_r \approx 40$ for fibroglandular tissue). Therefore, the effective wavelength and the resulting electric field distribution within the breast depend on density of fibroglandular tissue variations. In this study, the capability of the deep learning model to predict the electric field distribution from input dielectric properties was evaluated using an intentionally selected breast density model. To this end, a heterogeneously dense breast model derived from real MRI scans was obtained from the University of Wisconsin-Madison UWCEM repository [23]. To increase data variability for the learning process, the 3D breast model was divided into 107 individual 2D cross-sectional slices. These 107 slices represent different samples with varying geometries and tissue distributions, comprising seven segmented tissue types (e.g., skin, different fat compositions, and fibroglandular tissue). To improve the generalizability of the deep learning model and increase data variability, different dielectric properties were assigned to the tissues types based on [23]. The dielectric properties were computed using the Cole–Cole equation (1) with the parameters in Table I. Calculations were performed from 0.8 to 5 GHz in 0.2 GHz steps (22 frequency points), increasing the dataset size from 107 to 107 × 22 samples.

$$\varepsilon^*(\omega) = \varepsilon_\infty + \frac{\varepsilon_s - \varepsilon_\infty}{1+(j\omega\tau)^{(1-\alpha)}} + \frac{\sigma_s}{j\omega\varepsilon_0} \qquad (1)$$

where $\varepsilon^*(\omega)$ is complex permittivity; ε_s and ε_∞ denote the static permittivity and infinite-frequency permittivity, respectively. τ is relaxation time and α is distribution parameter (0–1). σ_s and ε_0 are ionic conductivity and vacuum permittivity. ω denotes angular frequency.

Table 1. Cole-Cole parameters for the dielectric property characterization of breast tissues [23].

Type	ε_∞	$\Delta\varepsilon$	$\tau\ (ps)$	α	$\sigma_s(S/m)$
minimum	2.293	0.141	16.40	0.251	0.002
Fat type 1	2.908	1.200	16.88	0.069	0.020
Fat type 2	3.140	1.708	14.65	0.061	0.036
Fat type 3	4.031	3.654	14.12	0.055	0.083
Fibroglandular type 1	9.941	26.60	10.90	0.003	0.462
Fibroglandular type 2	7.821	41.48	10.66	0.047	0.713
Fibroglandular type 3	6.151	48.26	10.26	0.049	0.809
maximum	1.000	66.31	7.585	0.063	1.370

A total of 2,354 unique 2D samples were generated, where each sample corresponds to a different case characterized by a distinct anatomical geometry and dielectric property map. This process is referred to as dielectric modulation during input data generation (Fig. 1).

The slices of the breast model were positioned within a square area measuring 120 mm × 120 mm, referred to as the Region of Interest (ROI). A 3D line source was expressed as a 2D point source in the FEM-based electromagnetic calculation. The source which had a magnitude of 1 V and was oriented in the x-direction, was located at the border of the ROI (at x = -60 mm), represented mathematically as $\vec{E}(x,y) = \delta(x-60)\vec{x}$ V/m. A scattering boundary condition was established to ensure the source and the ROI are enclosed. The 2D EF distributions generated within the

breast model by this source was calculated for 2354 slices, and these distributions were accepted as the ground truth for the study, forming the output dataset.

A fixed set of boundary conditions was used across all FEM simulations to ensure consistency in data generation. Specifically, the scattering boundary conditions were applied to the outer edges of the simulation domain to mimic open-space behavior and minimize artificial reflections. The DL models were trained to implicitly learn the mapping between dielectric property distributions and the resulting EF under this specific boundary condition setup. While this controlled configuration supports stable model training and evaluation, generalization to scenarios involving different boundary conditions remains a subject for future investigation.

Additionally, the data size requirement was analyzed by decreasing the training dataset randomly to 75%, 50%, 25%, and 10%. The electrical conductivity (S/m), relative permittivity, and the corresponding EF (V/m) distribution of an example data, the 115^{th} instance of the test dataset, are demonstrated in Fig. 2, where a color gradient transitioning from blue to red represent these properties with conductivity from 0 to 3 S/m, relative permittivity ranging from 0 to 50 and EF distribution from 0 to 0.8 V/m.

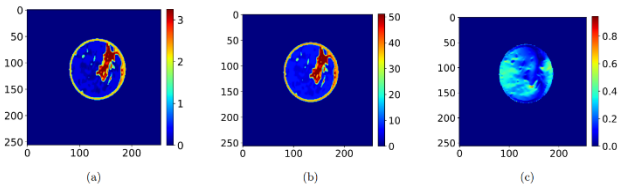

Figure 2. Prepared sample data for input and output: (a) the conductivity (S/m) and (b) permittivity distributions of the 115^{th} test instance, and (c) the corresponding EF distribution (V/m) obtained via finite element method (FEM).

Deep learning

In this study, deep learning models based on UNet [22] and ResNeXt50 [21,24] architectures have been developed to predict the electrical field from input data of conductivity and permittivity, chosen for their simplicity to demonstrate the feasibility of the proposed approach as a foundational study. The ResNeXt50 model serves as a foundational feature extractor due to its grouped convolutional design, which enhances its ability to learn complex patterns. To adapt ResNeXt50 for this task, the initial convolutional layer was modified to accept two input channels, reflecting the nature of our input data. Additionally, the fully connected and average pooling layers were removed to maintain spatial resolution throughout the network, and a final convolution layer was added to produce a single-channel output that predicts the electrical field. However, ResNeXt50 alone does not inherently excel at image-to-image translation tasks, necessitating further architectural adjustments.

To enhance the performance of ResNeXt50 in dense prediction tasks, we integrated its backbone into a UNet architecture, which combines powerful feature extraction with the encoder-decoder structure of UNet. The UNet model with the ResNeXt50 backbone utilizes downsampling and upsampling pathways to refine the extracted features into precise spatial predictions. This configuration effectively leverages the strengths of both architectures, processing two input channels representing conductivity and permittivity to generate a single output channel predicting the electrical field. The integrated approach preserves detailed spatial information, enhancing the network's ability to produce accurate and contextually rich outputs. For brevity, the UNet model with a ResNeXt50 backbone will hereafter be referred to as R50-UNet, while the unmodified ResNeXt50 model will be denoted as R50.

For model training, the mean squared error (MSE) loss function was initially employed. To improve the learning process, a masking method was utilized in the loss calculation to focus on significant areas by creating a mask of non-zero values from the input data. The Adam optimization algorithm, with a learning rate of 0.0001 and weight decay of $1 - e^5$, was used to minimize overfitting and control the learning speed. A mini-batch size of 16 was chosen to optimize memory usage and enhance the model's generalization capability, and training was conducted over 200 epochs. This setup aims to capture complex patterns in the dataset and improve generalization performance, with hyperparameters carefully tuned to align with the problem definition and dataset characteristics.

Masking method

In our framework, the masking method plays an important role in improving the training efficiency and prediction accuracy of the deep learning models. Rather than computing the loss over the entire input, which includes large regions of background (typically air), we selectively focus on the regions of interest. This is accomplished by generating a binary mask that identifies non-zero values in the input data—specifically, the first channel containing electrical conductivity. Since the background exhibits zero conductivity, the mask effectively isolates the tissue regions where the EF is actually present.

By applying this mask during loss calculation, the model's learning process is directed towards the significant areas, thereby minimizing the impact of irrelevant background noise. This targeted loss evaluation not only accelerates convergence but also improves the robustness and accuracy of the predictions. The detailed procedure for mask creation and its application in the custom loss function is provided in Algorithms 1 and 2.

Evaluation metrics

First of the utilized evaluation metrics for model performance is the MSE and the average squared difference between the two-dimensional predicted and actual values was used to evaluate reconstruction or prediction quality.

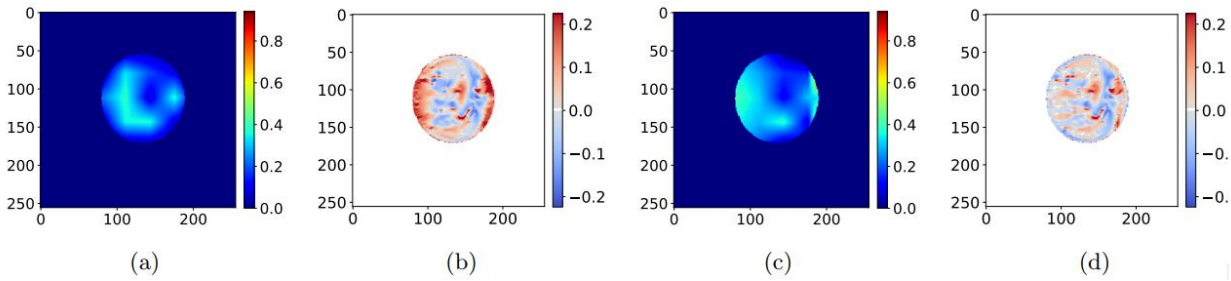

Figure 3. The prediction results of the standard and the R50 with masked loss models of 115^{th} test instance. FEM-computed EF distribution (V/m) (Ground truth) is given in Fig. 2. (a) The EF (V/m) prediction obtained by the standard model; (b) the difference distribution between the standard model prediction and the ground truth; (c) the EF (V/m) prediction obtained by the model with masked loss; (d) the difference distribution between the model with masked loss prediction and the ground truth.

Algorithm 1. Mask creation

1: Input: *Input data tensor i, shape* [batch_size, channel, height, width]

2: Output: *Generated mask m*

3: $m \leftarrow (i \neq 0)$.any(dim = 1, keepdim=True).float()

4: Creates a mask for non-zero values across inputs

5: return *m*

Algorithm 2. Custom loss function

1: Inputs: *Model output o, Target data t, Mask m*

2: Output: Calculated loss

3: $loss \leftarrow \frac{mse(o \cdot m,\ t \cdot m,\ reduction = 'sum')}{m \cdot sum()}$

4: Calculates MSE loss over the masked region

5: return *loss*

Pixel-wise MSE can be calculated as

$$MSE = \frac{1}{mn}\sum_{i=1}^{m}\sum_{j=1}^{n}\left(I_{ij} - K_{ij}\right)^2 \qquad (1)$$

where I and K represent the original and reconstructed 2D data, respectively, i and j are the pixel indices, and m and n are their dimensions. However, when the error values are less than one, then MSE produces very small numbers, making it difficult to analyze. Therefore, RMSE is calculated to examine the difference between the predicted values and the actual values, expressed in the units of the prediction data. RMSE can be calculated as

$$RMSE(y, \hat{y}) = \sqrt{\frac{\sum_{i=1}^{N}(y_i - \hat{y}_i)^2}{N}} \qquad (2)$$

where y_i and $\hat{y}_i$ denote the predicted and the observed value, respectively. N is the total number of data points. Additionally, the MAE measures the accuracy of a prediction model by averaging the absolute differences between predicted and actual values. A lower MAE signifies better prediction accuracy. MAE can be calculated as

$$MAE = \sum_{i=1}^{N}|y_i - \hat{y}_i|. \qquad (3)$$

Another evaluation metric for model performance is the (SNR). SNR is a general metric used to measure the quality of model outputs and their resilience to noise [25]. The theoretical formulation of SNR is as follows:

$$SNR(y, \hat{y}) = 10\log_{10}\left(\frac{\sum_{i=1}^{N}(y_i)^2}{\sum_{i=1}^{N}(y_i - \hat{y}_i)^2}\right). \qquad (4)$$

SNR is calculated as the decimal logarithm of the ratio of the power of the exact reference signal to the power of the difference between the signal and the prediction. This criterion objectively assesses the quality of the outputs produced by the model and how resilient they are to noise.

Results and Discussion

This study conducted a comprehensive evaluation of deep learning model performance, specifically focusing on the R50 and R50-UNet architectures, in predicting EF distributions within breast tissue. The key metrics for this evaluation includes RMSE, MAE, and SNR. The analysis utilized a dataset consisting of 2,354 instances, with 2,208 allocated for training and 146 for testing.

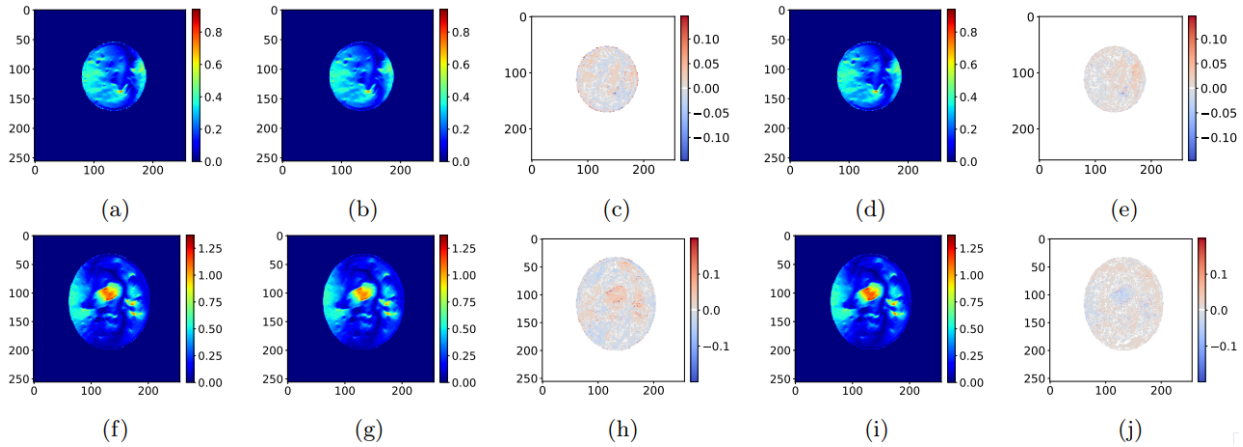

Figure 4. The prediction results of the standard and the R50-UNet model with masked loss for 115^{th} test instance: (a) FEM-computed EF distribution (V/m) of 115^{th} test instance (Ground truth); (b) the EF (V/m) prediction obtained by the standard model; (c) the difference distribution between the standard model prediction and the ground truth; (d) the EF (V/m) prediction obtained by the model with masked loss; (e) the difference distribution between the model with masked loss prediction and the ground truth. (f-j) The prediction results of the standard and the R50-UNet model with masked loss for 19^{th} test instance.

These results are referred to as representing 100% of the dataset (Data %) in the text and the tables. The baseline model employed the standard R50 architecture with a standard MSE loss function, while the R50 model with masked loss function incorporated a masking method in the loss calculation. Predictions of both models were gathered using the 2D conductivity and permittivity data (displayed in Fig. 2) of the 115^{th} instance of the test dataset. The EF distribution obtained via FEM, which serves as the ground truth, is shown in Fig. 2c. The prediction from the standard R50 model for the 115^{th} instance is illustrated in Fig. 3a, and the difference between the ground truth and the prediction is depicted in Fig. 3b. In these difference maps (Figure 3b and 3d), red indicates regions where the predicted value is higher than the ground truth, blue represents areas where the predicted value is lower than the ground truth, and white denotes pixels where the prediction closely/exactly matches the ground truth. The evaluated metrics for this prediction yield RMSE of 0.0402 V/m, MAE of 0.0121 V/m, and SNR of 8.1405 dB. The 115^{th} instance demonstrated the highest performance across the test dataset, while Table 2 lists the average metrics across the entire test dataset as 0.0750±0.0197, 0.0317±0.0102, and 6.61±0.63 dB for SNR.

The R50 model with masked loss prediction for the 115^{th} instance is shown in Fig. 3c, with the difference between the ground truth and the prediction visualized in Fig. 3d. The calculated metrics for this instance are RMSE of 0.0294 V/m, MAE of 0.0085 V/m, and SNR of 10.855 dB. The R50 model with masked loss exhibited a 27% reduction in RMSE, a 30% reduction in MAE, and a 33% increase in SNR compared to the standard model. As detailed in Table 2, applying the masking technique in the training loss function for the R50 model enhanced the overall EF distribution prediction performance across the test dataset, leading to decreases in RMSE and MAE by 0.0152 V/m and

Table 2. The prediction performance results for the R50 model with the standard and masked loss function calculations applied on systematically reduced datasets. Root Mean Square (RMSE), Mean Absolute Error (MAE), and Signal-to-Noise Ratio (SNR) metrics metrics averaged over the test dataset are presented.

R50 Model	Data %	RMSE (V/m)	MAE (V/m)	SNR (dB)
Standard	100	**0.0750 ± 0.0197**	0.0317 ± 0.0102	6.61 ± 0.63
	75	0.0750 ± 0.0199	**0.0316 ± 0.0103**	**6.62 ± 0.65**
	50	0.0753 ± 0.0198	0.0318 ± 0.0102	6.59 ± 0.66
	25	0.0757 ± 0.0199	0.0329 ± 0.0109	6.53 ± 0.65
	10	0.0772 ± 0.0196	0.0331 ± 0.0103	6.34 ± 0.59
Masked	100	**0.0598 ± 0.0183**	0.0240 ± 0.0084	8.67 ± 0.98
	75	0.0599 ± 0.0185	0.0239 ± 0.0084	8.68 ± 1.02
	50	0.0599 ± 0.0185	**0.0238 ± 0.0083**	**8.68 ± 1.01**
	25	0.0601 ± 0.0184	0.0240 ± 0.0084	8.64 ± 0.99
	10	0.0667 ± 0.0181	0.0284 ± 0.0092	7.66 ± 0.88

0.077 V/m, respectively, and an average improvement in SNR of 2.07 dB. The best metric for each model is given in bold in Table 2, where the data is given in the format of *mean±standard deviation*.

Another model, R50-UNet, was analyzed for its input-output prediction capability using both the standard and masked loss functions during the training phase. The visual prediction results for the 115^{th} test instance are shown in Fig. 4a-4e. The standard R50-UNet achieves an RMSE of 0.0110 V/m, an MAE of 0.0024 V/m, and an SNR of 19.30 dB, while the R50-UNet model with masked loss yields an RMSE of 0.0071 V/m, an MAE of 0.0018 V/m, and an SNR of 23.14 dB. These metrics indicate superior prediction performance compared to the R50 models, with the R50-UNet model with masked loss achieving the best results. Fig. 4f-4j presents the 19^{th} test instance, which features a different slice of breast tissue with different size and distributions of conductivity and permittivity. For this instance, the standard R50-UNet metrics are 0.0156 V/m RMSE, 0.0054 V/m MAE, and 21.40 dB SNR, while the R50-UNet model with masked loss metrics are 0.0110 V/m RMSE, 0.0038 V/m MAE, and 24.41 dB SNR.

Table 3 presents the average RMSE, MAE, and SNR values for both the standard and R50-UNet model with masked loss across the entire test dataset. The average metrics for the test dataset are as follows: RMSE of 0.0157±0.0058 V/m, MAE of 0.0058±0.0019 V/m, and SNR of 20.09±0.68 dB. These results highlight the superior predictive accuracy of the R50-UNet model with masked loss compared to the standard R50-UNet model, as well as both the standard and R50 with masked loss models. Notably, the R50-UNet model with masked loss achieves the lowest RMSE and MAE values while attaining the highest SNR, indicating its ability to more precisely estimate EF distributions with reduced error and improved signal quality. The effectiveness of the masking approach in enhancing performance is evident from these results. For clarity, the best-performing metric for each model is highlighted in bold in Table 3, further emphasizing the advantages of the R50-UNet model with masked loss over the alternatives.

Furthermore, to understand the data size requirements for the models, the training data size was reduced to 75%, 50%, 25%, and 10% through random data selection. The models for each architecture were re-trained with these varying data percentages, and the corresponding prediction metrics are listed in Tables 2 and 2 for R50 and R50-UNet, respectively. For the R50 models, performance metrics at data sizes up to 25% varied by approximately 1% or less, whereas utilizing only 10% of the training data resulted in a significant drop in performance. Specifically, the average SNR of the R50 model with masked loss predictions decreased by 0.98 dB when using 10% of the training set, although the performance loss was less pronounced for the standard R50 model. Notably, the prediction metrics for the R50 model with masked loss with 10% data outperformed those of the standard R50 model, even when using 100% of the data. Further increasing the data size with these models is unnecessary, as the prediction performance saturates after training on 25% of the data.

The impact of dataset size on R50-UNet models is more significant compared to R50 models. For the standard R50-UNet, the SNR declines by 0.04 dB, 1.41 dB, 3.19 dB, and 7.09 dB when using 75%, 50%, 25%, and 10% of the data, respectively. Similarly, for the R50-UNet model with masked loss, the SNR decreases by 0.77 dB, 2.49 dB, 4.52 dB, and 7.61 dB across the same data reductions. These results suggest that expanding the dataset could further enhance the R50-UNet model with masked loss's predictive performance, as the SNR trends indicate that saturation has not yet been reached. In literature, Yao et al. [17, 18] trained deep learning models, such as DConvNets and DRCNN, using EF distributions derived from the MNIST dataset, evaluating their performance on cylindrical objects. Their approach initially focused on modeling Green's function for a single frequency before expanding to a broadband range, achieving NMSE values of 0.005 and 0.0004. In contrast, the present study directly models EF distributions within a fixed antenna system based on dielectric properties, eliminating the need for Green's function modeling. By incorporating realistic datasets, such as breast tissue obtained from MRI scans, this approach improves clinical feasibility by enabling efficient EF computations in environments with constant incident fields. RMSE of

Table 3. The prediction performance results for the thR50-UNet model with the standard and masked loss function calculations applied on systematically reduced datasets. RMSE, MAE, and SNR metrics averaged over the test dataset are presented.

R50-Unet Model	Data %	RMSE (V/m)	MAE (V/m)	SNR (dB)
Standard	100	0.0157 ± 0.0034	0.0058 ± 0.0019	**20.09 ± 0.68**
	75	**0.0157 ± 0.0033**	**0.0058 ± 0.0017**	20.05 ± 1.03
	50	0.0184 ± 0.0038	0.0069 ± 0.0022	18.68 ± 0.74
	25	0.0227 ± 0.0051	0.0088 ± 0.0030	16.90 ± 0.88
	10	0.0355 ± 0.0076	0.0147 ± 0.0046	13.00 ± 1.10
Masked	100	**0.0108 ± 0.0025**	**0.0039 ± 0.0012**	**23.33 ± 0.67**
	75	0.0118 ± 0.0027	0.0043 ± 0.0014	22.56 ± 0.69
	50	0.0145 ± 0.0036	0.0055 ± 0.0019	20.84 ± 0.80
	25	0.0184 ± 0.0050	0.0072 ± 0.0027	18.81 ± 1.11
	10	0.0264 ± 0.0076	0.0109 ± 0.0042	15.72 ± 1.57

0.0157 and 0.0108 for the UNet models with the standard and the masked loss functions translate to 0.0002 and 0.0001 NMSE values.

For a 2D MRI-derived breast slice excited by the EF source, each R50-UNet model generates predictions in approximately 0.02 s. Extrapolating to eight sources and six components of the complex EF vector yields a total computation time of about 0.96 s when predictions are computed sequentially. This time could be significantly reduced if predictions are computed in parallel. On the same computer used in the proposed model, FEM with a maximum mesh element size of 15 mm requires 11.42 s to compute the EF for eight sources and six components. When extended to a 3D model consisting of 80 slices, the total prediction time increases to approximately 76.8 s (0.96×80) using R50-UNet, whereas the corresponding FEM computation time increases to about 913.6 s (11.42×80), highlighting the substantial computational efficiency of the proposed approach.

Conclusion

In conclusion, this study demonstrates the efficacy of deep learning models, specifically R50-UNet and R50, in accurately predicting two-dimensional EF distributions from dielectric properties. By significantly reducing computation time more than 10-folds, our approach addresses the challenges associated with traditional numerical methods, particularly in static systems where complexity can hinder analysis. The incorporation of a masking-based loss function further enhances model performance, enabling focused learning on critical regions of interest and yielding substantial improvements in signal-to-noise ratios. Notably, the R50-UNet model outperformed R50, highlighting its suitability for this application. While the R50 model reached saturation in prediction accuracy with a reduced dataset, the R50-UNet model shows potential for further enhancement with larger datasets. This research not only underscores the transformative potential of deep learning in medical applications but also lays the groundwork for future studies to refine and expand upon these methodologies, ultimately improving the precision and efficiency of EF distribution predictions in clinical settings.

This study may be improved by implementing more than one breast model to increase the learning ability of the model. Furthermore, models based on different breast densities may be preferred as they have the potential to provide more accurate predictions. Additionally, the study should be translated into three-dimensional breast models to mimic real-life clinic settings. Therefore, as this study serves as a feasibility study for predicting EF distribution in a complex anatomical breast model, future work will focus on developing models capable of predicting EF distributions in both 2D and 3D using a larger and more diverse set of breast models. Moreover, while the current study is limited to predicting the real part of the x-component of the electric field, future extensions will aim to predict all components of the electric field vector (x, y, z), including both real and imaginary parts, to enable a more comprehensive and physically accurate representation of the field. Apart from these, the deep learning framework can be extended by incorporating tumor-containing datasets to evaluate its potential to assist in distinguishing tumor-induced changes in EF distribution.

Ethics committee approval and conflict of interest statement

There is no need to obtain permission from the ethics committee for the article prepared

There is no conflict of interest with any person / institution in the article prepared

Acknowledgements

This work was supported by the Scientific and Technological Research Council of Türkiye (TÜBİTAK) under Project No.125E412, and by the Scientific Research Projects (BAP) Coordination Unit of Istanbul Technical University (ITU) under Project No. MAB-2023-44842.

References

[1] A. Janjic, I. Akduman, M. Cayoren, O. Bugdayci, and M. Aribal, “Safe—microwave imaging device for breast cancer early screening and diagnostics,” in *Electromagnetic Imaging for a Novel Generation of Medical Devices: Fundamental Issues, Methodological Challenges and Practical Implementation*, 2023, pp. 273–292.

[2] E. Maheshwari et al., “Update on MRI in evaluation and treatment of endometrial cancer,” *Radiographics*, vol. 42, pp. 2112–2130, 2022.

[3] G. Altintas, I. Akduman, A. Janjic, and T. Yilmaz, “A novel approach on microwave hyperthermia,” *Diagnostics*, vol. 11, p. 493, 2021.

[4] H. Kasban, M. El-Bendary, and D. Salama, “A comparative study of medical imaging techniques,” *Int. J. Inf. Sci. Intell. Syst.*, vol. 4, pp. 37–58, 2015.

[5] B. Acar, T. Y. Abdolsaheb, and A. Yapar, “Advanced hyperthermia treatment: optimizing microwave energy focus for breast cancer therapy,” *Turk. J. Electr. Eng. Comput. Sci.*, vol. 32, pp. 268–284, 2024.

[6] A. Turgut and B. Engiz, “Analyzing the SAR in human head tissues under different exposure scenarios,” *Appl. Sci.*, vol. 13, p. 6971, 2023.

[7] A. Hirata et al., "Assessment of human exposure to electromagnetic fields: Review and future directions," *IEEE Trans. Electromagn. Compat.*, vol. 63, pp. 1619–1630, 2021.

[8] N. Iacob, "Pitfalls and challenges in specific absorption rate evaluation for functionalized and coated magnetic nanoparticles used in magnetic fluid hyperthermia," *Coatings*, vol. 15, p. 345, 2025.

[9] F. Kahnert, "Numerical methods in electromagnetic scattering theory," *J. Quant. Spectrosc. Radiat. Transfer*, vol. 79, pp. 775–824, 2003.

[10] M. N. Sadiku, *Numerical Techniques in Electromagnetics with Matlab*, 3rd ed. Boca Raton, FL, USA: CRC Press, 2012.

[11] J. Jin, *The Finite Element Method in Electromagnetics*, 3rd ed. Hoboken, NJ, USA: Wiley, 2015.

[12] R. Harrington, *Field Computation by Moment Methods*, New York, NY, USA: IEEE Press, 1993.

[13] S. Joof et al., "A guideline for complex permittivity retrieval of tissue-mimicking phantoms from open-ended coaxial probe response with deep learning," *IEEE Trans. Microw. Theory Techn.*, vol. 70, pp. 5105–5115, 2022.

[14] C. Aydinalp, S. Joof, M. Akinci, I. Akduman, and T. Yilmaz, "Microwave dielectric property retrieval from open-ended coaxial probe response with deep learning," *IEEE Access*, vol. 10, pp. 1216–1227, 2021.

[15] P. Wiecha and O. Muskens, "Deep learning meets nanophotonics: A generalized accurate predictor for near fields and far fields of arbitrary 3D nanostructures," *Nano Lett.*, vol. 20, pp. 329–338, 2019.

[16] M. Li and Z. Ma, "Accurate prediction of electric fields of nanoparticles with deep learning methods," *IEEE J. Multiscale Multiphysics Comput. Tech.*, vol. 8, pp. 178–186, 2023.

[17] H. M. Yao, L. Jiang, and M. Ng, "Implementing the fast full-wave electromagnetic forward solver using the deep convolutional encoder-decoder architecture," *IEEE Trans. Antennas Propag.*, vol. 71, no. 1, pp. 1152–1157, 2022.

[18] H. M. Yao, L. Jiang, and M. Ng, "Enhanced deep learning approach for electromagnetic forward modelling of dielectric target within the wide frequency band using deep residual convolutional neural network," *IEEE Antennas Wireless Propag. Lett.*, vol. 23, no. 6, pp. 1884–1888, 2024.

[19] S. Ayyachamy, V. Alex, M. Khened, and G. Krishnamurthi, "Medical image retrieval using ResNet-18," in *Proc. SPIE Med. Imaging: Imaging Informatics Healthcare Res. Appl.*, San Diego, CA, USA, 2019, pp. 233–241.

[20] D. Sarwinda, R. Paradisa, A. Bustamam, and P. Anggia, "Deep learning in image classification using residual network (ResNet) variants for detection of colorectal cancer," *Procedia Comput. Sci.*, vol. 179, pp. 423–431, 2021.

[21] S. Xie, R. Girshick, P. Dollár, Z. Tu, and K. He, "Aggregated residual transformations for deep neural networks," in *Proc. IEEE Conf. Comput. Vis. Pattern Recognit.*, Honolulu, HI, USA, 2017, pp. 1492–1500.

[22] O. Ronneberger, P. Fischer, and T. Brox, "U-Net: Convolutional networks for biomedical image segmentation," in *Proc. MICCAI*, Munich, Germany, 2015, pp. 234–241.

[23] E. Zastrow, S. Davis, M. Lazebnik, F. Kelcz, B. Van Veen, and S. Hagness, "Database of 3D grid-based numerical breast phantoms for use in computational electromagnetics simulations," Dept. Elect. Comput. Eng., Univ. Wisconsin-Madison, Madison, WI, USA, 2007.

[24] K. He, X. Zhang, S. Ren, and J. Sun, "Deep residual learning for image recognition," in *Proc. IEEE Conf. Comput. Vis. Pattern Recognit.*, Las Vegas, NV, USA, 2016, pp. 770–778.

[25] J. G. Proakis, *Digital Signal Processing: Principles, Algorithms, and Applications*, 4th ed., Upper Saddle River, NJ, USA: Pearson, 2007.